

# Application of large eddy simulation models to electroconvection turbulence study with lattice Boltzmann method

Yu Zhang, Kang Luo, and Hongliang Yi <sup>\*</sup>

*School of Energy Science and Engineering, Harbin Institute of Technology,  
Harbin 150001, People's Republic of China*

*and Key Laboratory of Aerospace Thermophysics, Ministry of Industry and Information Technology,  
Harbin 150001, People's Republic of China*

Anjun Liu

*Jinan Key Laboratory of High Performance Industrial Software,  
Jinan Institute of Supercomputing Technology, Jinan 250353, People's Republic of China*

Jian Wu 

*School of Energy Science and Engineering, Harbin Institute of Technology,  
Harbin 150001, People's Republic of China*



(Received 11 April 2024; accepted 15 July 2024; published 28 August 2024)

Electroconvection (EC) turbulence is an important branch of electrohydrodynamics (EHD). Because the turbulence model for EHD has not been well studied, in this work we apply the large eddy simulation (LES) to electrohydrodynamic turbulence based on the lattice Boltzmann method (LBM). The eddy-viscosity methods (the Smagorinsky and wall-adapting local eddy-viscosity models) are used to model the momentum equation, and the charge transport equation is modeled with the help of the turbulent Schmidt number. Three EC cases are chosen to test the reliability of the LBM-LES models, including two-dimensional (2D) EC turbulence in square and rectangular cells, and three-dimensional (3D) EC turbulence between two parallel plates. For 2D cases, the LES results are compared to the results of different numerical methods, including direct numerical simulation and LES. The long-time statistics of maximum velocity, charge current and its probability distribution, and flow evolution are used to validate the 2D EC turbulence. We also analyze the flow patterns and average characteristics for 3D cases. The LES results could capture the main flow features of EC turbulence for all cases, and demonstrate a good agreement when compared with references. The mentioned LBM-LES models have demonstrated reliability and high computational speed, making them suitable for further simulations of electrohydrodynamic turbulence.

DOI: [10.1103/PhysRevFluids.9.083703](https://doi.org/10.1103/PhysRevFluids.9.083703)

## I. INTRODUCTION

Turbulence appears in ubiquity and affects the performance of many industrial devices [1]. Turbulent convection can be triggered by driven forces coupled with multiphysical fields, like heat convection [2–7], magnetohydrodynamic flow [8–11], and electrohydrodynamic flow [12–16]. Among them, numerous engineering applications, for example, electrostatic spraying [17,18], electrohydrodynamic enhancement of phase-change heat transfer [19–21], demineralization [22–25],

---

<sup>\*</sup>Contact author: yihongliang@hit.edu.cn

and electrohydrodynamic ion-drag pumps [26–28], are derived from electrohydrodynamic phenomena. Electrohydrodynamics (EHD) is an interdisciplinary subject that involves interaction between hydrodynamics and electric force at least [20]. The study of EHD encompasses the investigation of practical applications and the exploration of in-depth physical mechanisms. An important aspect of the latter is to study the complicated fluid physics in EHD, including flow stability, transition, and turbulence.

Electroconvection (EC), a classic model of EHD, is employed to investigate the fluid mechanics in electrodriven flow. The electrodriven convection may be induced when a strong enough bias electric field is imposed on metal-liquid interfaces [12,29,30]. Free electric charge is generated by charge injection, and the charge is driven by the electric force and flow convection, causing strong coupling between multiscale forces [31]. Castellanos [29] reviewed the charge injection EC flow elaborately in their work, including important results of theoretical analysis and experiment. These foundational conclusions provide ideas for further studying charge injection EC turbulence.

EC turbulence is an important topic in electrohydrodynamic study. Hopfinger and Gosse [32] and Lacroix *et al.* [12] performed related experiments on electrohydrodynamic turbulence in early studies, deriving several scaling laws and characteristic scales of charge injection turbulence. Zhang [33] carried out experimental studies to investigate temporal, spatial, spectral, and correlational electro-optic signatures of turbulent EC. Their study provides some new possibilities in technique to further study EC turbulence. Tsai *et al.* [14,15] studied electrohydrodynamic turbulence in annular film electroconvection, comparing the results with Grossmann-Lohse theory in heat buoyancy-driven turbulence [34] to construct a unified scaling law. Varshney *et al.* [35] and Wang *et al.* [16,36,37] investigated the velocity power spectrum of turbulence in the electrokinetic flow, finding an additional length scale in electrohydrodynamic turbulence.

Besides experiments, numerical simulation is a powerful tool in electrohydrodynamic turbulence study. Kourmatzis and Shrimpton [38] performed a series of numerical works on EC turbulence, showing the basic phenomena of three-dimensional (3D) turbulence. Traoré and Pérez [39] investigated the influence of charge mobility and electric Rayleigh number on two-dimensional (2D) EC, which introduces a high-driven parameter study of EC. Recently, Wang *et al.* [40], Huang *et al.* [41], and Zhang *et al.* [42] studied the 2D EC turbulence in different geometries and boundary conditions, involving the evolution of power spectrum density, electric Nusselt number, and energy budget in the EC system. However, we notice that the previous numerical studies of EC turbulence are all based on direct simulation without the help of any turbulence models, which restricts the study area of EC simulation.

Although several numerical studies on EHD involve a significant interplay between the electric field and turbulence, the application of electrohydrodynamic turbulence models is confined to a few scenarios. Kourmatzis and Shrimpton [43] demonstrated the Reynolds stress method (RSM) close in free electroconvection, resulting in a reasonable accuracy. To the best of the authors' knowledge, there are no further related studies. It is well known that there are various turbulence models after long years of development. The most typical types are, e.g., Reynolds-averaged Navier–Stokes equations (RANS) and large eddy simulation (LES) [1,44]. The former describes the average features of turbulence. RANS-like models contribute excellently to industry. However, for investigating the particular hydrodynamics mechanisms in electrohydrodynamic flow, we need a more detailed description of the flow. Therefore, it is essential to develop and take advantage of some kind of LES models in the EHD turbulence study, which could conserve most of the flow details and keep the numerical cost in an acceptable scope.

This work aims to implement an LES model in EC turbulence simulation. We employ the Smagorinsky subgrid method for the electrohydrodynamic study and investigate the effectiveness of such an LES model in EC turbulence simulation [45–47]. Moreover, the wall-adapting local eddy-viscosity (WALE) model [48] is also employed to perform a comparison. In the past decades, the finite volume method (FVM) and lattice Boltzmann method (LBM) both have been widely used in electrohydrodynamic research [38,39,49–54]. The LBM is simple and efficient in computation, and it is easy to implement in parallel, especially on heterogeneous computing platforms [55–59].

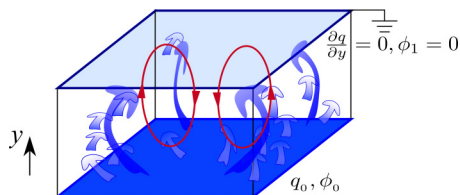


FIG. 1. A sketch of the charge injection convection.

It also has demonstrated versatility and stability in multiphysics and complex fluids [60,61]. In addition, the LBM is a transient method with low numerical dissipation, making it widely used in turbulence simulation work [55,62,63]. Rooted in the reasons mentioned above, we decided to employ the LBM as the numerical solver in this study. And we also compare the result of the LBM with the FVM in the computational results and speed, for comprehensive studying since they are all spatial second-order precision numerical methods.

Turbulence simulation based on the LBM has experienced rapid development since the subgrid model and Reynolds-averaged turbulence models were incorporated into the LBM [45,46]. The LES-LBM approach is widely employed in numerical simulation of multiphysics turbulence. Chen *et al.* [64] performed a numerical study of turbulent double-diffusive natural convection in a square cavity with the aid of an LBM-LES model. Meanwhile, LBM-LES models were also used for the simulation of thermal convection turbulence [65–70]. In these studies, the eddy viscosity is realized by adjusting the lattice relaxation time, and different LES models coupled with a few lattice Boltzmann (LB) schemes are tested by the researchers. In addition, Flint and Vahala [71] proposed an LBM-LES model for magnetohydrodynamic simulation. Their work realizes the subgrid viscosity computation by adjusting the equilibrium moment rather than correcting the relaxation time by nonequilibrium distribution functions, which indicates the flexibility of realization of subgrid viscosity in the LBM. Recently, Taha *et al.* [72] used an LES model in a compressible LBM for the simulation of forced plumes. In summary, the abundant researches reflect the potential of LBM-LES models for multiphysics electrohydrodynamic turbulence simulation.

We discuss the application of the LBM-LES models in turbulent EC simulation in this work, including the Smagorinsky model and the WALE model in EC turbulence simulation. And we consider three kinds of cases, including 2D and 3D flows, to test the LES models. The rest of this paper is organized as follows. We introduce the EC physical model and governing equations and then present the numerical method and LES implementation in Sec. II. The numerical results and discussions are presented in Sec. III. In Sec. IV, we summarize the effect of using the LBM-LES models in EC turbulence simulation and provide some prospects for EC turbulence simulation.

## II. PHYSICAL MODEL AND NUMERICAL REALIZATION

The physical model sketch is shown in Fig. 1. We consider the unipolar charge injection EC problem between two plate electrodes [30,39,73]. The work medium is incompressible, Newtonian, and dielectric liquid. The liquid layer is subjected to an external electric field by imposing a high voltage  $\phi_0$  on the lower plate and a ground potential  $\phi_1$  on the upper plates. Complicated electrochemical reactions may take place at the electrode-liquid interface, generating electric charges and causing charge injection towards the bulk from the high-voltage electrode. The liquid motion may go through a dynamic evolution from hydrostatic to laminar and further develop into chaotic states. In the study of EC, we examine hydrodynamic phenomena and charge transfer, while omitting the consideration of the charge generation mechanism. The discharge mechanism of the EC model is assumed to be homogeneous and autonomous charge injection, and the charge quantity on the electrode is represented as  $q_0$ . In addition, the electric double layer effect at walls is also ignored.

We assume by default that the vertical direction is represented by  $y$ , and  $x$  (and  $z$ , if in the 3D case) for the horizontal direction.

### A. Governing equations of EC

The physical governing equations of the electrohydrodynamic problem consist of the Poisson equation, the charge transfer equation (or a specific form of the Nernst-Planck equation), and the incompressible Navier-Stokes (NS) equations, respectively [13,74]. The characteristic scales in the system are chosen as follows: electric drift time  $H^2/(K\phi_0)$  for time; the height of the liquid layer,  $H$ , for length; the difference of voltage,  $\Delta\phi = (\phi_0 - \phi_1)$ , for electric potential; the density of the dielectric liquid,  $\rho_0$ , for density; the charge density on the electrode surface,  $q_0$ , for the charge; and  $\rho K^2(\phi_0 - \phi_1)^2/H^2$  for pressure, respectively. Here,  $K$  and  $\rho$  are ion mobility and dielectric liquid density. With the above dimensionless scales, the corresponding equations are derived, namely [13,39,42],

$$\nabla \cdot \mathbf{u} = 0, \quad (1)$$

$$\frac{\partial \mathbf{u}}{\partial t} + \mathbf{u} \cdot \nabla \mathbf{u} = -\nabla p + \frac{M^2}{T} \nabla^2 \mathbf{u} + CM^2 q \mathbf{E}, \quad (2)$$

$$\nabla^2 \phi = -Cq, \quad (3)$$

$$\mathbf{E} = -\nabla \phi, \quad (4)$$

$$\frac{\partial q}{\partial t} + \nabla \cdot (q\mathbf{E}) + \mathbf{u} \cdot \nabla q = \frac{M^2}{T} \frac{1}{\text{Sc}} \nabla^2 q, \quad (5)$$

where  $\mathbf{u}$ ,  $\mathbf{E}$ ,  $p$ ,  $q$ ,  $t$ , and  $\phi$  denote the velocity of liquid, electric field, modified pressure, charge density, time, and voltage, respectively. There are four nondimensional control parameters: the electric Rayleigh number  $T$ , the charge injection strength  $C$ , the mobility parameter  $M$ , and the electric Schmidt number  $\text{Sc}$ , which are defined by

$$T = \frac{\epsilon \Delta \phi}{\rho_0 \nu K}, \quad C = \frac{q_0 L^2}{\epsilon \Delta \phi}, \quad M = \frac{1}{K} \left( \frac{\epsilon}{\rho} \right)^{1/2}, \quad \text{Sc} = \frac{\nu}{D}, \quad (6)$$

in which  $\epsilon$ ,  $\nu$ , and  $D$  represent the permittivity, kinematic viscosity of the dielectric liquid, and charge-diffusion coefficient, respectively. It is noted that the electric Schmidt number is related to the dimensionless charge diffusion coefficient  $\alpha = D/(K \Delta \phi)$  by  $\alpha = M^2/(T \text{Sc})$ . The passing charge current can be quantified through the charge flux  $I_e$ , and the electric Nusselt number  $\text{Nu}_e$  is defined as

$$\text{Nu}_e = \frac{I_e}{I_0}, \quad I_e = \frac{1}{V} \int_V \left[ qE_y + qu_y - \frac{1}{\text{Sc}} \frac{M^2}{T} \frac{\partial q}{\partial y} \right] dV. \quad (7)$$

where  $I_0$  is the dimensionless charge current at the hydrostatic state under the same electric-driven parameter. The three components in the right-hand side of Eq. (7) correspond to electric drift  $I_E$ , convection  $I_v$ , and diffusion  $I_D$  mechanisms, which will be used in the discussion.

### B. The LES models for EC turbulence

The backbone of LES is the introduction of a spatial filtering to decompose a variable  $v(\mathbf{u}, p, q, \phi)$  into a filtered component  $\bar{v}$  and a residual component  $v'$ , that is,  $\bar{v} = v - v'$ , which can smooth out variable fluctuations on the order of filter width  $\Delta$  [1,44]. The filtered equations resemble

Reynolds-averaged equations but the cross terms of filtered variables remain. We list the filtered subgrid-scale electrohydrodynamic equations below using the tensor notation,

$$\frac{\partial \bar{u}_i}{\partial x_i} = 0, \quad (8)$$

$$\frac{\partial \bar{u}_i}{\partial t} + \frac{\partial \bar{u}_i \bar{u}_j}{\partial x_j} = -\frac{1}{\rho} \frac{\partial \bar{p}}{\partial x_i} + \frac{M^2}{T} \frac{\partial^2 \bar{u}_i}{\partial x_j \partial x_j} + CM^2 \bar{q} \bar{E}_i + CM^2 (\bar{q} \bar{E}_i - \bar{q} \bar{E}_i) - \frac{\partial (\bar{u}_i \bar{u}_j - \bar{u}_i \bar{u}_j)}{\partial x_j}, \quad (9)$$

$$\frac{\partial \bar{q}}{\partial t} + \frac{\partial \bar{q} \bar{u}_i}{\partial x_i} + \frac{\partial \bar{q} \bar{E}_i}{\partial x_i} = \frac{M^2}{T} \frac{1}{Sc} \frac{\partial^2 \bar{q}}{\partial x_j \partial x_j} - \left( \frac{\partial (\bar{q} \bar{u}_i - \bar{q} \bar{u}_i)}{\partial x_i} + \frac{\partial (\bar{q} \bar{E}_i - \bar{q} \bar{E}_i)}{\partial x_i} \right), \quad (10)$$

$$\frac{\partial^2 \bar{\phi}}{\partial x_j \partial x_j} = -C \bar{q}, \quad (11)$$

$$\bar{E}_i = \frac{\partial \bar{\phi}}{\partial x_i}, \quad (12)$$

in which the crucial question is to deal with the nonlinear terms of filtered variables, which are included in parentheses. These nonlinear terms include the effects of the small-scale eddies that have been truncated due to coarse graining and are not resolved in LES.

First, the Smagorinsky model is used to evaluate the term of the residual stress of the momentum equation [44]. An eddy viscosity is introduced to close the equation,

$$\nu_t = (C_s \Delta)^2 (|\bar{S}|^2)^{\frac{1}{2}}, \quad (13)$$

where  $|\bar{S}| = (2\bar{S}_{ij}\bar{S}_{ij})^{1/2}$  is the characteristic filtered rate of strain, with  $\bar{S}_{ij} = 1/2 (\partial \bar{u}_i / \partial x_j + \partial \bar{u}_j / \partial x_i)$ ,  $C_s$  the Smagorinsky coefficient, and  $\Delta$  is fixed because the LBM uses a uniform mesh. The Smagorinsky model can be coupled naturally in the lattice collision step. In addition, we would like to introduce the WALE model that could decay the dissipation near the walls, to enrich comparison. The WALE model is expressed as follows:

$$\nu_t = (C_w \Delta)^2 \frac{(S_{ij}^d S_{ij}^d)^{3/2}}{(\bar{S}_{ij} \bar{S}_{ij})^{5/2} + (S_{ij}^d S_{ij}^d)^{5/4}}, \quad (14)$$

in which  $S_{ij}^d = 1/2(\bar{g}_{ij}^2 + \bar{g}_{ji}^2) - 1/3\delta_{ij}\bar{g}_{kk}^2$  is the traceless symmetric part of the square of the velocity gradient tensor, where  $C_w$  is a constant that is adjustable according to practical problems,  $\bar{g}_{ij} = \partial \bar{u}_i / \partial x_j$  and  $\bar{g}_{ij}^2 = \bar{g}_{ik}\bar{g}_{kj}$ . For the charge transport equation, we use the turbulent Schmidt number  $Sc_t = \nu_t / D_t$  [64,75,76], which is defined by the ratio of the eddy viscosity  $\nu_t$  to the eddy diffusivity  $D_t$ , to estimate the additional effect of filtered terms. Since the Poisson equation is linear, we maintain the original formula while replacing the original variables with the filtered ones.

### C. Lattice Boltzmann equations

We accomplish the LES model in lattice Boltzmann equations (LBEs) for solving different partial differential equations in the EC system. To balance numerical stability and calculation efficiency, the multirelaxation time (MRT) scheme is employed for solving the flow field, and the charge transport and Poisson equations are solved using the single-relaxation time (SRT) scheme. For convenience, the LB distribution functions directly represent the filtered variables, and the overline symbols are omitted.

The MRT LBE for the flow field reads [61]

$$f_i(\mathbf{x} + \mathbf{c}_i \delta_t, t + \delta_t) = f_i(\mathbf{x}, t) - (\mathbf{M}^{-1} \mathbf{S} \mathbf{M})_{ij} [f_j(\mathbf{x}, t) - f_j^{eq}(\mathbf{x}, t)] + \delta_t \mathbf{M}^{-1} \left( \mathbf{I} - \frac{\mathbf{S}}{2} \right) \mathbf{M} \tilde{\mathbf{F}}, \quad (15)$$

where  $\mathbf{x}$ ,  $\delta_t$ ,  $f_i$ ,  $f_i^{eq}$ , and  $\tilde{\mathbf{F}}$  denote the lattice node position, the LBE evolution time step, the distribution function, the equilibrium distribution function, and the external force distribution

function computed by the scheme proposed by Guo *et al.* [77], respectively. Here the external force term in the force distribution function is  $\bar{\mathbf{F}} = CM^2\bar{q}\bar{\mathbf{E}}$  in Eq. (9).  $\mathbf{M}$  is the orthogonal transformation matrix from the LB velocity space to moment space, and  $\mathbf{S}$  is the relaxation matrix [61,73,78,79]. The equilibrium distribution function  $f_i^{eq}$  reads

$$f_i^{eq} = w_i\rho\left(1 + \frac{\mathbf{c}_i \cdot \mathbf{u}}{c_s^2} + \frac{(\mathbf{c}_i \cdot \mathbf{u})^2}{2c_s^4} - \frac{\mathbf{u} \cdot \mathbf{u}}{2c_s^2}\right), \quad (16)$$

where  $\mathbf{c}_i$  is the lattice discrete velocity for the flow field LBE, and  $c_s = c/\sqrt{3}$  is the speed of sound in lattice units. The macroscopic density and velocity are defined by the first second-order moments of the distribution function, namely,  $\rho = \sum_i f_i$  and  $\bar{\mathbf{u}} = (\sum_i \mathbf{c}_i f_i + \frac{\delta_t}{2}\bar{\mathbf{F}})/\rho$ .

The LES model is used to handle the residual nonlinear terms  $CM^2(\overline{qE_i} - \bar{q}\bar{E}_i)$  and  $(\partial\bar{u}_i\bar{u}_j - \bar{u}_i\bar{u}_j)/\partial x_j$  in the filtered NS equation. The effect of these terms is substituted by an effective eddy viscosity, as shown in Eq. (13) or Eq. (14). For the Smagorinsky model, to determine the strain rate tensor  $\bar{S}_{ij}$ , we evaluate the second-order moment of the nonequilibrium distribution function in the LBM rather than computing the gradient of the filtered velocity directly [45,47], which reads

$$\begin{aligned} S_{ij} &= -\frac{1}{2\rho c_s^2 \tau \delta_t} \sum_{\alpha} \mathbf{c}_{\alpha i} \mathbf{c}_{\alpha j} [f_{\alpha}(\mathbf{x}, t) - f_{\alpha}^{eq}(\mathbf{x}, t)] \\ &= -\frac{1}{2\rho c_s^2 \delta_t} \sum_{\alpha} \mathbf{c}_{\alpha i} \mathbf{c}_{\alpha j} \sum_{\beta} (\mathbf{M}^{-1} \mathbf{S} \mathbf{M})_{\alpha\beta} [f_{\beta}(\mathbf{x}, t) - f_{\beta}^{eq}(\mathbf{x}, t)], \end{aligned} \quad (17)$$

where  $\tau$  is the relaxation time of the LBE. We could get the stress tensor through the distribution function or distribution moment, which depends on the programming realization. If we use the WALE mode, the corresponding tensors are computed after the LB collision steps. It consumes additional finite difference to compute the velocity gradient, and handles several tensor computations. After getting the effective eddy viscosity, we can obtain the turbulence viscosity. Then the term  $\omega_v$  in the relaxation matrix is determined, and the viscosity-related term satisfies

$$\tau = \frac{1}{\omega_v} = \frac{M^2/T + \nu_t}{c_s^2 \delta_t} + \frac{1}{2}, \quad (18)$$

in which  $M^2/T + \nu_t$  is the effective viscosity of the subgrid method.

The evolution equation of the charge density is based on the advection-diffusion equation (ADE) LBE, which is written as

$$g_i(\mathbf{x} + \mathbf{c}_i \delta_t, t + \delta_t) = g_i(\mathbf{x}, t) - \frac{1}{\tau_g} [g_j(\mathbf{x}, t) - g_j^{eq}(\mathbf{x}, t)], \quad (19)$$

where  $g_i$ ,  $g_i^{eq}$ , and  $\tau_g$  are the distribution function, the equilibrium distribution function, and the relaxation time, respectively. Here,  $g_i^{eq}$  reads

$$g_i^{eq} = w_i q \left(1 + \frac{\mathbf{e}_i \cdot \mathbf{u}}{c_{s,q}^2}\right), \quad (20)$$

where  $\mathbf{e}_i$  is the lattice discrete velocity for the charge transport and Poisson LBE. The macroscopic charge density  $q$  is obtained by taking the zero-order moment of the distribution function  $q = \sum_i g_i$ .

The relaxation time  $\tau_g$  is related to the dimensionless charge diffusivity  $M^2/(TSc_t)$  and the turbulence diffusivity  $D_t$ . The turbulent Schmidt number  $Sc_t$  is used to evaluate the turbulent diffusivity of the charge transport equation, that is,  $D_t = \nu_t/Sc_t$ . Therefore, the relaxation time of

the charge transport equation LBE is

$$\tau_g = \frac{M^2/(TSc) + D_t}{c_{s,g}^2 \delta_t} + \frac{1}{2}, \quad (21)$$

where  $c_{s,g}$  is the lattice sound speed of the ADE LBE. The macroscopic charge density  $\bar{q}$  in Eq. (11) is obtained by taking the zero-order moment of the function  $q = \sum_i g_i$ .

Compared to the charge density field, the potential field is more stable and smooth. Here, the Poisson LBE proposed by Chai and Shi [80] is employed to solve Eq.(10), which reads

$$\varphi_i(\mathbf{x} + \mathbf{e}_i \delta_t, t + \delta_t) - \varphi_i(\mathbf{x}, t) = -\frac{1}{\tau_\phi} [\varphi_i(\mathbf{x}, t) - \varphi_i^{eq}(\mathbf{x}, t)] + \delta_t \varpi_i R D_\phi, \quad (22)$$

where  $\tau_\phi$  is the relaxation time,  $R$  is the right-hand term in Eq. (10),  $D_\phi = \alpha c^2 (\frac{1}{2} - \tau_\phi) \delta_t$  is the artificial diffusion coefficient, and  $\varpi_i$  is the weight factor for the source term discretization which satisfies  $\sum_i \varpi_i = 1$ . The equilibrium distribution function is defined by

$$\varphi_i^{eq} = \begin{cases} (\omega_0 - 1)\varphi(\mathbf{x}, t), & i = 0 \\ \omega_i \varphi(\mathbf{x}, t), & i \neq 0. \end{cases} \quad (23)$$

The voltage is evaluated by  $\phi = \frac{1}{1-w_0} \sum_i \varphi_i$ , in which  $w_i$  is the weight factor of the equilibrium distribution function. We do not need to deal with the Poisson equation by using any subgrid model because the potential is related to the charge density directly. The electric field can be evaluated by  $\mathbf{E} = -\nabla \phi = 1/(\tau_\phi \delta_t \alpha) \sum_i \mathbf{e}_i \varphi_i$ . So far, we have briefly introduced our LBM-LES model and implementation for electrohydrodynamic simulation.

#### D. Numerical implementation

The LBM-LES model for EHD is developed based on the open-source platform Palabos [78], which has helped fulfill several simulation studies on EHD [21,73,79]. In this paper, we perform both 2D and 3D EC simulations through the current LBM-LES model. The LBE of the NS equations is solved using the D2Q9 and D3Q19 models, respectively. And the charge transport equation and the Poisson equation are implemented with the aid of the D2Q5 and D3Q7 models. The Smagorinsky coefficient  $C_s$  is set as 0.17, and the WALE model constant  $C_w$  is 0.5 [81,82]. Involving the turbulent Schmidt number of the charge transport equation, we analogized the choice of simulating thermal convection [65,67–69] and did a series of numerical tests about  $Sc_t$ . Finally, we found the statistics of EC turbulence are not sensitive to  $Sc_t$ . We set the turbulence Schmidt number to 0.4, slightly underestimating it to ensure the numerical stability. Because there is a large difference in value between the viscosity and charge diffusivity while the relaxation time of LBEs is coupled strongly with these two variables, we set the LB evolution time step of the NS equation to be smaller than that of the charge transport equation, that is,  $\delta_{t,D} = k \delta_{t,v}$ . This could stabilize the LBE iteration and reduce the computational time. After massive numerical tests, we advise to set  $k$  as  $\sim 5$ –10. The resolutions are set based on experience tests and compared with the Kolmogorov and Batchelor length scales [38],  $\eta$  and  $\eta_B$ , ensuring the LES numerical grids could not resolve the smallest scale well. In EC, the two scales can be computed through  $\eta/l \sim (2700/M)^{3/8} (MR)^{-3/4}$  [29] and  $\eta_B = (\eta/Sc^{1/2})$  [83,84], in which  $l$  is the length of a characteristic large-scale EC eddy. Furthermore, we conducted *a posteriori* validation about the root mean square horizontal velocity of all results, confirming that there is no need to introduce a wall function model in this work.

### III. RESULTS AND DISCUSSION

This work selects several examples fulfilled by previous numerical works as comparisons. In this section, we present three numerical cases, namely, the 2D EC flow in a square domain and a rectangular region with an aspect ratio of 0.614, and the 3D EC turbulence between two plate domains. The Smagorinsky model is used for all cases while the WALE model is employed in the

TABLE I. The grid resolution of results computed by different numerical models, and the comparison between the grid scale and turbulent smallest scale. The computations based on the Smagorinsky and WALE models (including the comparison with FVM) share the same resolution. Here the characteristic length of a large-scale eddy in 2D EC turbulence is assumed to be the same as the cavity height [42].

$T$	LES(LB,FV)	$\eta/\Delta$	$\eta_B/\Delta$	LBM+DNS	SEM+DNS
5000	201 <sup>2</sup>	0.065	0.648	513 <sup>2</sup>	40×48(8 <sup>2</sup> )
10 000	321 <sup>2</sup>	0.068	0.681	769 <sup>2</sup>	60×64(8 <sup>2</sup> )
20 000	401 <sup>2</sup>	0.092	0.916	1025 <sup>2</sup>	80×84(8 <sup>2</sup> )
30 000	501 <sup>2</sup>	0.099	0.993	1337 <sup>2</sup>	90×96(8 <sup>2</sup> )
40 000	769 <sup>2</sup>	0.080	0.802	2049 <sup>2</sup>	100×112(8 <sup>2</sup> )

first case. The side wall boundary conditions for 2D cases are all no slip, and the lateral boundary conditions of 3D cases are periodic. All of the showing results are collected in statistically steady conditions.

### A. 2D EC turbulence in a square cavity

In this section, we show the numerical results for the 2D EC flow in a square cavity with the Rayleigh number ranging from 5000 to 40 000, and other parameters are  $M = 10$ ,  $C = 10$ , and  $Sc = 100$ , respectively. The study adopts both LBM-LES (based on the Smagorinsky and the WALE models) and direct numerical simulation (DNS) to simulate this case, where the DNS is fulfilled through the LBM and the continuous Galerkin spectral element method (CG-SEM), which is performed in the free software Nek5000 [42,85–88]. The computation of the FVM is performed in the platform OpenFOAM-9 [89,90], and the WALE model parameters are the same as those in the LBM simulation. The total variation diminishing (TVD) schemes [39,49] and Euler backward time discretization are employed to maintain numerical stability and computational speed.

Table I shows the resolutions of all of the computations. To compare the ability to capture different charge transfer mechanisms for the five methods, Fig. 2 presents the temporal averages of charge current, which are divided into three mechanisms of diffusion  $I_D$ , electric drift  $I_E$ , and convection  $I_v$ . Figure 3 illustrates the temporal averages of the electric Nusselt number and the

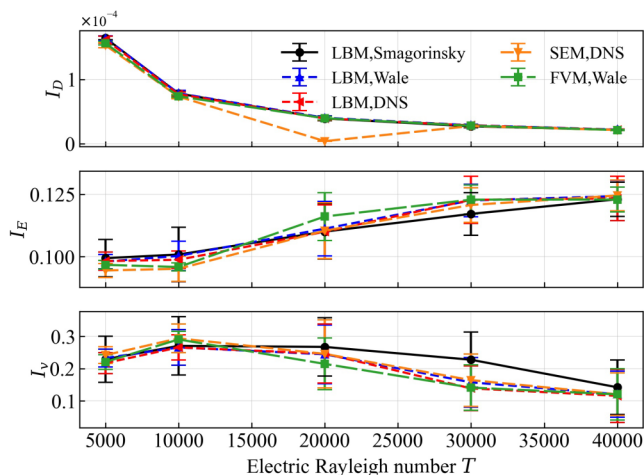


FIG. 2. The comparison of time averages of each component of current, i.e., diffusion  $I_D$ , electric drift  $I_E$ , and convection  $I_v$ . The error bars represent the standard deviation.

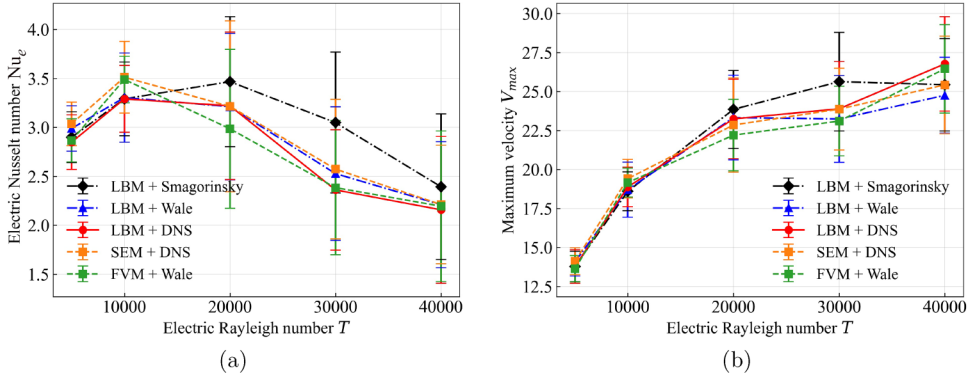


FIG. 3. Evolution of the maximum velocity and electric Nusselt number versus electric Rayleigh number  $T$ . The error bars represent the standard deviation.

maximum velocity. It is shown that the values of the five series of charge currents show a relatively good agreement, in particular for the diffusion and electric drift components. The  $Nu_e$  initially increases and then decreases as the electric Rayleigh number  $T$  rises. The LBM-LES models capture this trend clearly, with deviations all falling within the standard deviation range. The maximum velocity shows an increasing trend as  $T$  increases. And the difference of  $V_{max}$  between the LES and DNS results is smaller than that of  $Nu_e$ . It indicates that the two LES models can acquire reasonable convection intensity. However, there are a few aspects to improve to get a better feature of the electric Nusselt number, especially for the Smagorinsky model.

Although Fig. 2 indicates that the diffusion and electric drift components agree well with the DNS results, the convection components of the Smagorinsky model show a certain discrepancy at  $T = 30\,000$ . The biggest differences of  $Nu_e$  and  $V_{max}$  when  $T = 30\,000$  also appear in Fig. 3. To qualitatively compare the simulation results, we plot typical instantaneous snapshots of the results computed by the LBM-LES (Smagorinsky) and LBM-DNS models for  $T = 20\,000$ ,  $30\,000$ , and  $40\,000$  cases, as shown in Fig. 4. We observe slim mushroomlike charge plumes that are injected from the electrode below. The primary plumes move toward the upper plate by floating from the sidewalls and the central part of the plate below. Some more delicate plumes rotate with the EC vortices and dissipate in the bulk area of the cavity. For  $T = 30\,000$ , a single main roll occupies most of the space for both of the two results, as shown in Figs. 4(b) and 4(e). In Ref. [42], we proved that the single main cell mode appears more frequently after the  $T$  value exceeds  $20\,000$ . So in Figs. 4(c) and 4(f), we present the typical characters of a single cell mode at  $T = 40\,000$  for both LES and DNS results, which indicates that the LES model can capture the large-scale rolls of EC correctly. However, we can find that the dissipating plumes occupy less area in the LES results than in the DNS results; that is, more plume oscillations in the bulk are smeared by eddy viscosity. The phenomenon may be caused by the subgrid viscosity, providing additional dissipation under the insufficient mesh resolution.

Several time series and their probability density functions (PDFs) are shown in Fig. 5. The flow of the cases shown is fully turbulent and the time series exhibits high-frequency oscillations. And there is some intermittency, manifesting as quasiregular bursts and the obvious skewness of the PDF, especially for  $T = 20\,000$ . The previous work demonstrates that the intermittency is caused by the change of large-scale structure; for example, the two-main-cell pattern converts to a single-main-cell pattern, and the former has a higher energy utilization and charge transfer efficiency [42]. The case at  $T = 20\,000$  is dominated by electric force and behaves as the two-main-cell pattern. In contrast, the case  $T = 40\,000$  is dominated more by inertial force and has a higher proportion of the single-main-cell pattern. It should have a gradual transition of dominant flow mode in the parameter range  $T = 20\,000$ – $40\,000$ . Adopting the subgrid viscosity somewhat puts off the inertial force development

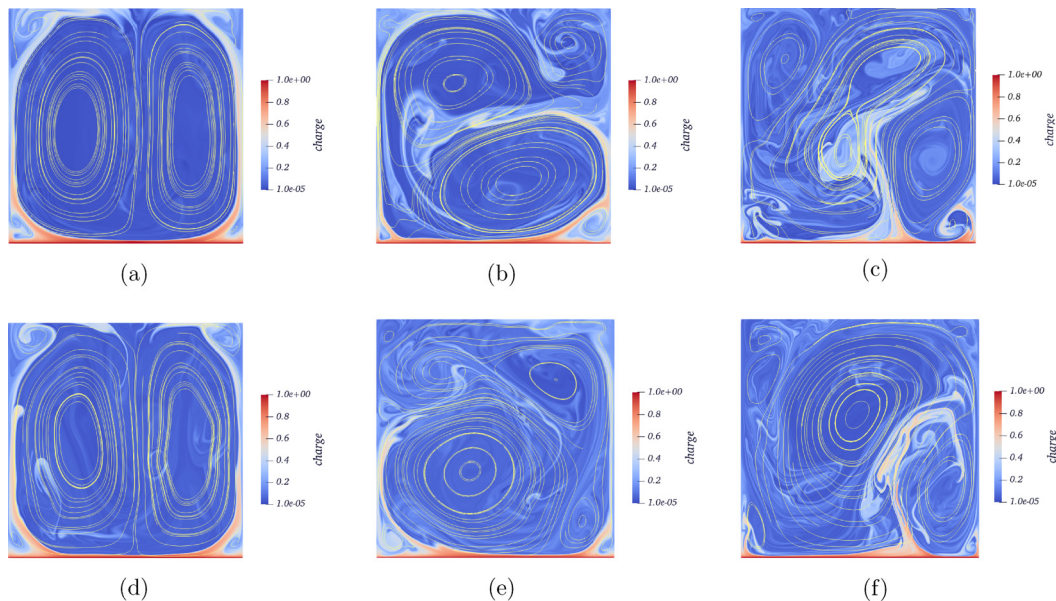


FIG. 4. Typical instantaneous snapshots of charge density and streamline at  $T = 20\,000$ ,  $30\,000$ , and  $40\,000$  (from left to right). [(a)–(c)] LBM-LES (by the Smagorinsky model) results; [(d)–(f)] LBM-DNS results.

(increases the effective viscosity). The phenomenon is especially evident in the Smagorinsky model; we think the reason is the eddy-viscosity effect near the walls. Thus, the result of the LBM-LES shows a higher charge transport efficiency and maximum velocity at  $T = 30\,000$ . Since the wall eddy viscosity is absent in the WALE model, the statistical results and PDFs seem closer to those of DNS. In addition, the ranges of PDFs of the FVM-WALE approach are narrower than the other results in most of the cases, that is, the smaller skewness. The FVM spatial discretization scheme has a bigger numerical diffusion compared to the LBM, which may decrease the exhibition of extreme situations, as shown in Figs. 5(a) and 5(b) obviously. Thus, our LBM-LES models may have a better performance for the electrohydrodynamic turbulence of a relatively low electric Rayleigh number. However, as turbulent models, the two series of LBM-LES result in this part all showing acceptable abilities to capture the overall flow and charge transport character.

At last, we want to talk about the computational efficiency of the LBM-LES model. The discussion only involves the computational efficiency for the LBM-DNS case, the LBM-LES models, and the FVM-WALE model, because the SEM model has a different numerical precision which makes it unrealistic to compare the computational speed quantitatively. The introduction of subgrid viscosity can decrease at least half of the resolution of DNS in a single direction. In addition, the computational time step is also at least twice the DNS time step. It is noted that the computation of the stress tensor in the LBM is straightforward by utilizing the nonequilibrium LB distribution functions. Thus, the theoretical speedup ratio of the Smagorinsky model compared to the LBM-DNS model is nearly eightfold. In practical simulations, we also find the speedup ratio is at least six- to eightfold compared with the DNS model for 2D cases, which depends on the computational core performance and number. Such a speedup ratio is crucial for the large-scale simulation of electrohydrodynamic flow. However, the computational efficiency of the WALE model is a little lower since the velocity gradient cannot be finished inside the LB collision step. After numerical tests, it would consume about an additional 3% of computational resource in the current cases because of some calculations of the tensor product in the WALE model. We also tested the computational times of the FVM-WALE model. If we set the same mesh resolution and time step,

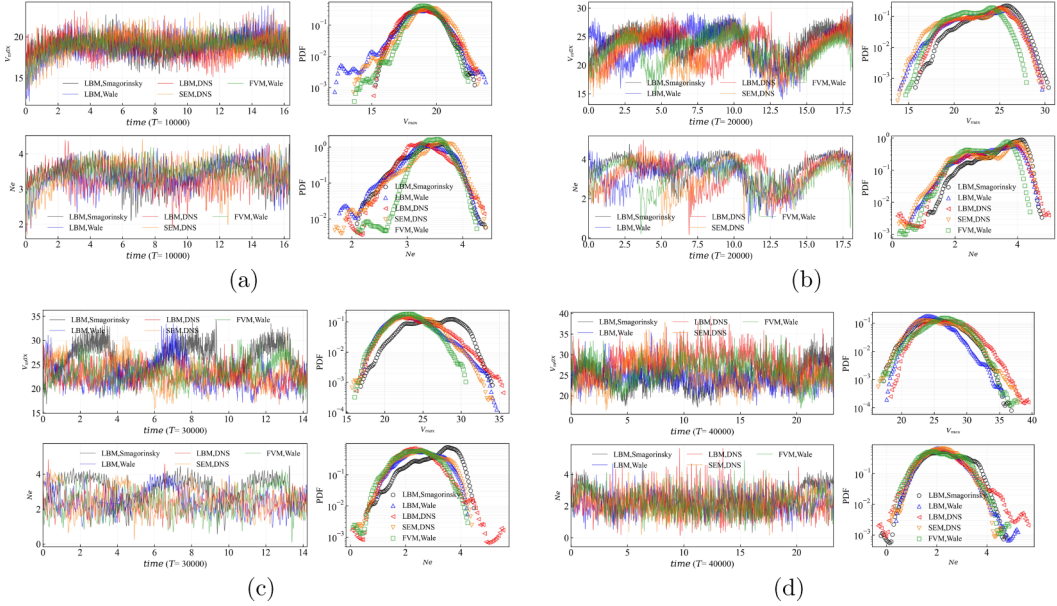


FIG. 5. Time series of electric Nusselt number and the maximum velocity and their PDFs at [(a)–(d)]  $T = 10\,000$ – $40\,000$  for all five methods.

the computational time is 6 to 19 times slower than that of the LBM-WALE model. And even though we set adaptive time for the FVM, the computational efficiency is also two to eight times slower. For larger-scale computation, like higher Rayleigh number EC which needs higher resolution, the advantage of the LBM in computational time can be more significant. In addition, to ensure the subgrid viscosity is necessary for the electrohydrodynamic turbulence simulation in a coarse grid, we tried to run the same case through the LBM-DNS model with half of the original grids; the numerical cases are easy to crush when the flow enters the turbulence-developing stage. This is because of the extremely low physical viscosity and diffusivity in the electrohydrodynamic model. It means the subgrid model stabilizes the numerical computation, which is essential for industrial computation.

## B. 2D EC turbulence in an enclosed rectangular cell

Then we simulate the electrohydrodynamic flow using the Smagorinsky model in an enclosed cell with an aspect ratio of 0.614. Similar cases were also tested by Traoré and Pérez [39] using the FVM. In our test, the electric Rayleigh number ranges from 10 000 to 50 000 in order to ensure the flow is sufficiently turbulent. In addition, the dimensionless mobility scope is  $\sim 10$ – $100$ . And this test adopts the no-slip boundary for all the walls. The mesh resolutions range from 241 to 1025 in the height direction depending on the driven parameters. The charge injection strength is 10 to represent the strong injection case. The electric Schmidt number  $Sc$  also changes from 100 to 1000, changing with charge mobility  $M$ ; i.e., for a small- $M$  cases, the electric  $Re$  is large, and we decrease  $Sc$  to 100 to balance the computational cost. The mentioned numerical setting can maintain the convection and electric drift as the dominant charge transport mechanisms for all of the numerical scenarios, which is essential for unipolar charge injection EC.

Figure 6 illustrates the evolution trends of maximum and electric Nusselt number with respect to electric Rayleigh number  $T$ . It can be seen that the maximum velocity always increases with the increase of  $T$ . In addition, the overall trend in velocity shows an increase with  $M$ . For the  $M = 10$  case, however, the velocity is notably lower than that of other instances. When  $M$  is larger than 30,

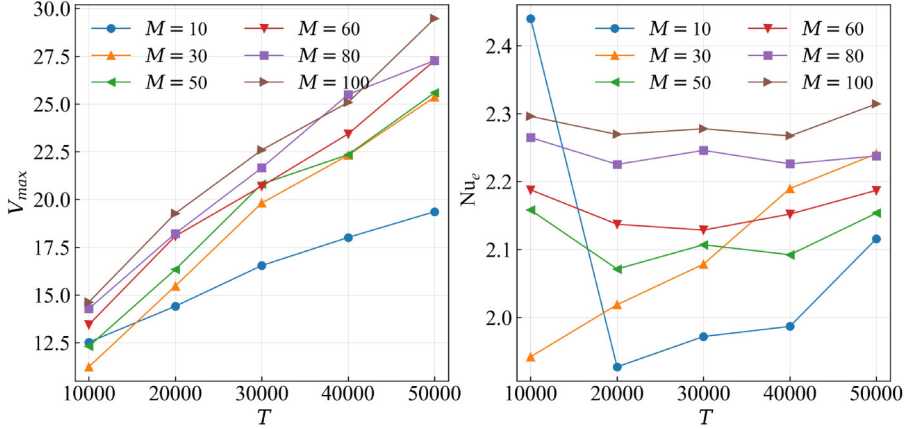


FIG. 6. Evolution of the maximum velocity and electric Nusselt number versus electric Rayleigh number  $T$ ; the results are computed at different  $M$  values.

the maximum velocity increases monotonously to the increase of  $M$ . The  $Nu_e$  also shows an increasing trend with respect to the rising  $T$  under the fixed  $M$  value, approaching saturation after  $T$  is large enough. However, there are a few abnormal cases, such as  $M = 10$  and  $30$ , presenting increasing trends of  $Nu_e$  with respect to  $T$  increasing. Traoré and Pérez [39] also gave similar results about the change of  $Nu_e$  with respect to  $M$  and  $T$ . Our results agree well with their results when  $M$  is larger than 30, all showing a saturated state with  $T$  increasing. Referring to the previous study about cavity electrohydrodynamic flow [42], it is possible to see an unstable change of  $Nu_e$  at a small  $M$  value. The reason is that the EC flow is more easily dominated by the inertial effect in these cases, resulting in a large range of fluctuation of charge flux. Nevertheless, our results also indicate that the 2D simulation result does not agree well with the  $Nu_e \sim M^{1/2}$  scaling law, which corroborates the previous study [39].

To further investigate the correctness of our LES model, we gather a series of DNS results computed by SEM at  $T = 50000$  for different  $M$  values, as shown in Fig. 7. Both sets of results are accompanied by their respective averages and standard errors. The average values are nearly identical and the errors overlap well, especially for  $M$  values larger than 30. In addition, the trends

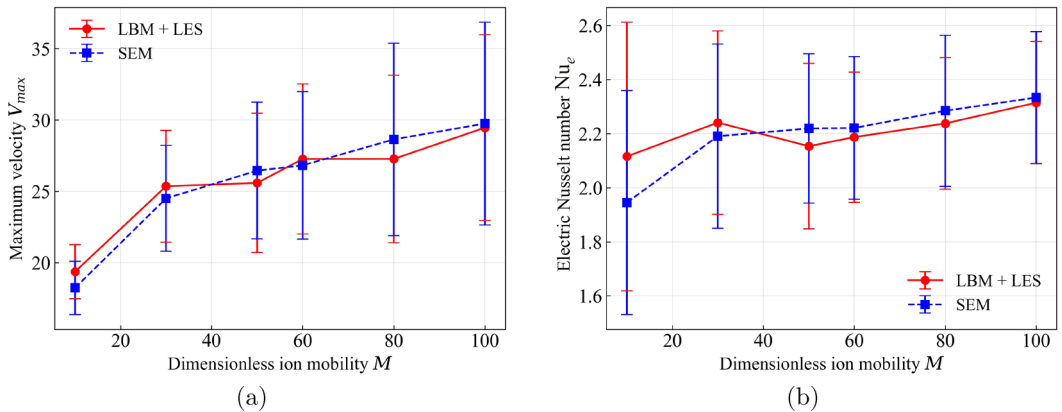


FIG. 7. The average values of maximum velocity and electric Nusselt number with the change of dimensionless ion mobility  $M$ , computed by LBM-LES and SEM models. The error bars represent standard deviations.

TABLE II. Simulation parameters for all cases with  $1 \times 5 \times 5$  numerical domain. The four cases (S1–S3 and S4) correspond to the setups of Kourmatzis and Shrimpton (S1–S3 and Sp) [38]. The characteristic large-scale length is computed through  $l \sim \sqrt{M/300}H$  [29] for computing the Kolmogorov scale. The resolution is the lattice number in vertical and two horizontal directions.

Case	$T$	$M$	$C$	Re	Resolution	$\eta/\delta_x$	$\eta_B/\delta_x$
S1	500	22.3607	10	1	$65 \times 320^2$	0.0975	0.9751
S2	500	2.8868	10	6	$73 \times 361^2$	0.5198	5.1979
S3	500	2.0412	10	120	$97 \times 481^2$	0.5280	5.2796
S4	1780	9.6791	4.6	19	$73 \times 361^2$	0.4674	4.6739

in the changes of  $V_{\max}$  and  $Nu_e$  also agree closely between the two sets of results. Because the SEM has a better accuracy whose result could be treated as a benchmark here, the result computed using LES is considerably effective in this context.

### C. 3D EC turbulence in the periodic domain

In this test, we simulate a series of 3D EC turbulence. The simulation parameters correspond to the work studied by Kourmatzis and Shrimpton [38], while all of the numerical domains are set as  $1 \times 5 \times 5$ . We list the control parameters and simulation resolution in Table II. To balance the simulation stability and computational cost, we set the electric Schmidt number as 100 for all cases.

Figure 8 shows the instantaneous velocity magnitude viewed on isosurfaces of charge density as well as vortex structures of EC. Figure 9 presents 2D slices of charge density at the midplane of the vertical direction. It is evident that all cases have entered at least chaotic or weak turbulence regimes. The charge density isosurfaces behave as irregular polygons and the vortices distribute along the charge isosurface. The polygonal charge cell boundaries of case S1 are nearly straight, while those of the other cases are more curved. The corresponding vortices of case S1 are coherent and large scale while the others are more dispersed and fragmented. Intuitively, it is apparent that the S1 and S4 cases exhibit higher convection intensity, so as the vorticity. Among them, the flow in case S4 is the most turbulent one, whereas case S1 displays a more orderly organization. Previous

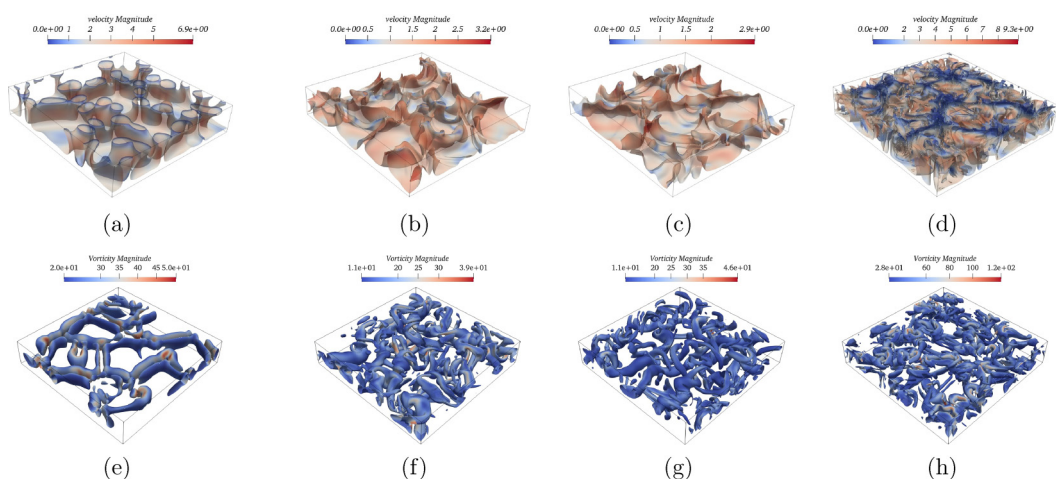


FIG. 8. [(a)–(d)] Velocity magnitude viewed on isosurfaces of the instantaneous charge density field of the four cases, where the isosurface charge density value is chosen as  $q = 0.15$ . [(e)–(f)] The vorticity  $Q$ -criterion field colored by vorticity magnitude at the same snapshots.

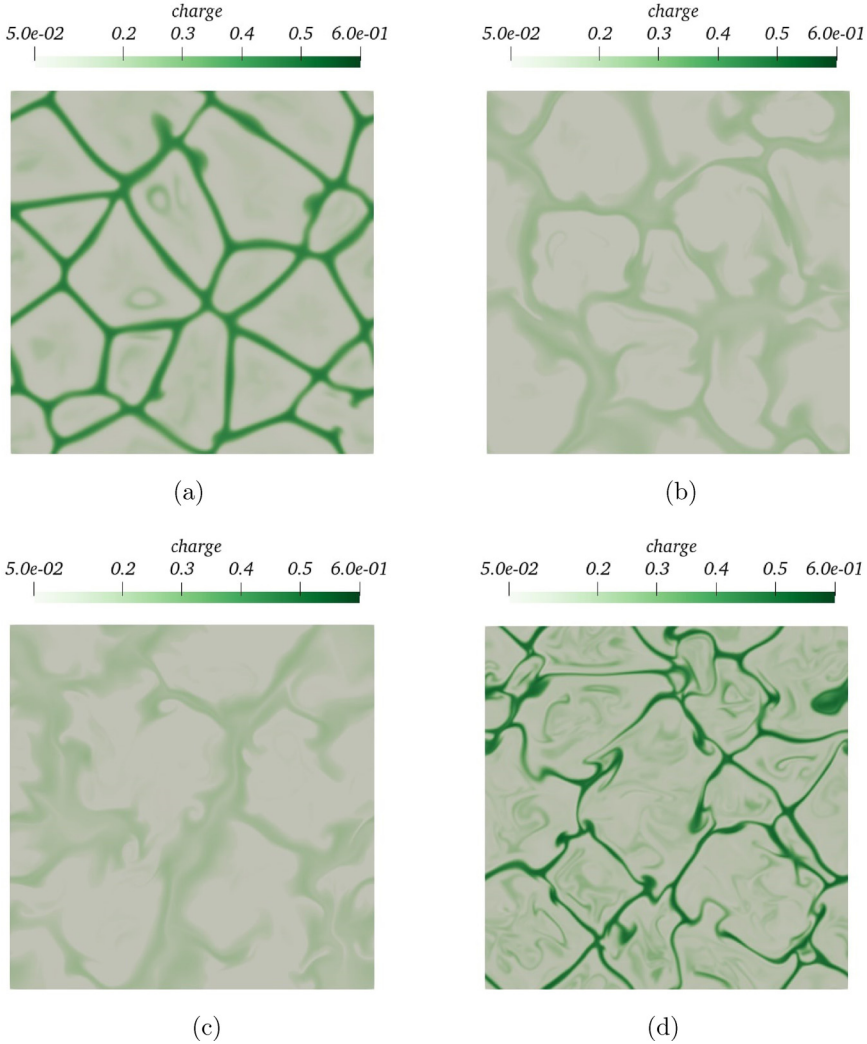


FIG. 9. Charge density distribution on the middle plate of the vertical direction.

works have revealed that for the 3D steady EC, the flow is more likely to develop as hexagonal structures [12,91,92]. Now, we can envision the flow patterns evolving with increasing electric Rayleigh numbers in 3D EC: initially, the flow patterns transition from relatively regular hexagons to polygons, and subsequently the structures become unordered, chaotic, and up to turbulent. In cases S1 and S4, the charge plumes have the capability to penetrate the bulk region, allowing them to easily float from the injection plate to the upper plate. Conversely, in cases S2 and S3, the plumes dissipate within the bulk region. Furthermore, we notice that the vortex distributions all follow the plumes' motion. Some plumes dissipate inside the charge void cells as the isolated vortices present here, too. This phenomenon can also be recognized from the charge density slice in the middle plate. The charge density of the plume area at this middle height is the highest in the S4 case while that becomes lower in cases S2 and S3. In previous 2D simulations, we could only see that the charge plumes float from the below plate. However, the current snapshots of charge density reveal that horizontal plumes can also split from upward plumes, as particularly evident in Figs. 9(b) and 9(c).

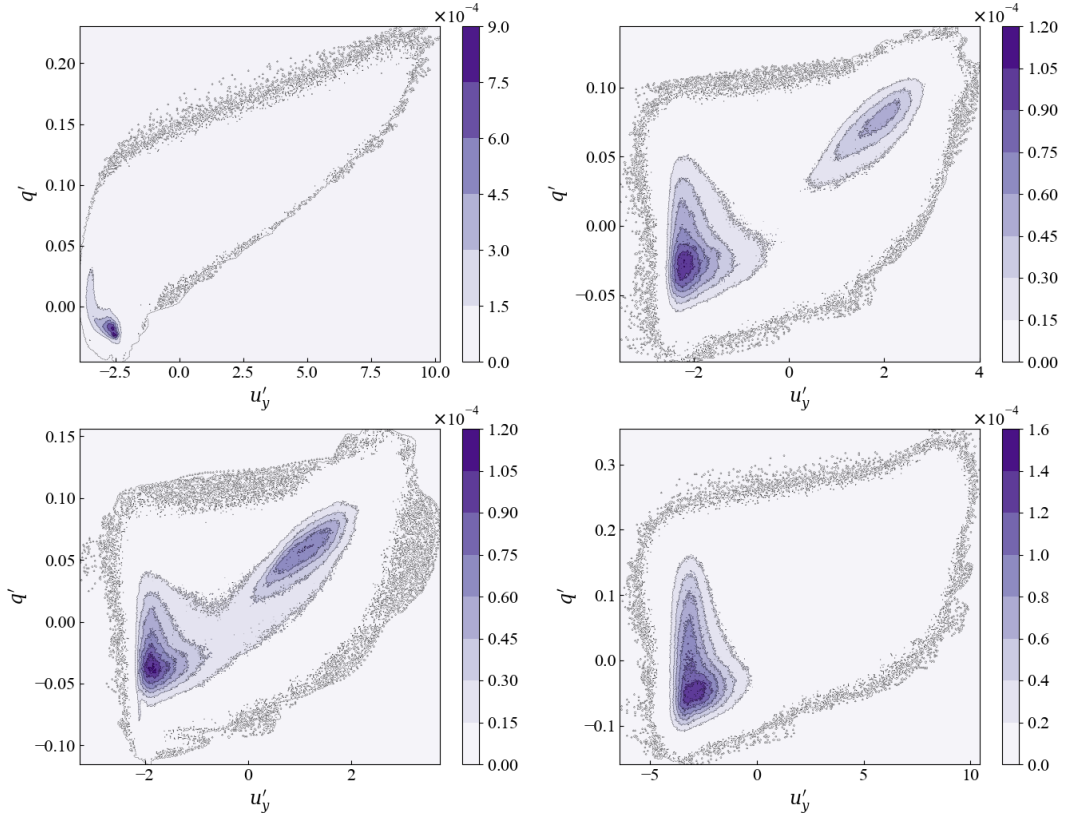


FIG. 10. Bivariate distributions of nondimensional vertical velocity fluctuations  $u'_y$  and charge fluctuations  $q'$  for all four cases.

Then we continue to analyze the bivariate probability distributions of charge fluctuation  $q'$  versus vertical direction velocity fluctuation  $u'_y$  calculated at  $y = 0.5d$ , using the notation  $(\cdot)' = (\cdot) - \langle (\cdot) \rangle_{s,t}$ , in which  $(\cdot)'$  is the fluctuation, and  $\langle (\cdot) \rangle_{s,t}$  is the spatial and temporal average of  $(\cdot)$  taken along the 2D plane over a series of realizations under statistically stationary conditions. As shown in Fig. 10, the bivariate distributions of the cases are not rigorously symmetric. The bivariate probability distribution of case S1 exhibits a single peak mode with a long tail, indicating high skewness. Similarly, the S4 case has a comparable trend but a broader charge fluctuation scope. This suggests that most charges are transported downwards, coinciding with the findings in Fig. 9. The area of peak probability of case S1 is more concentrated, which demonstrates that the flow in the case is more stable. The skewness is lower in cases S2 and S3, which show bimodality modes, reflecting that more upward flow appears in the conditions. Because these two cases show that the penetrability of the charge plumes is not as strong as in the S1 and S4 cases, the flow and charge density mixing at the middle plate could be more uniform. However, the downward flow is still dominant because of the existence of the electrical field. The findings in our results are in good agreement with those of Kourmatzis and Shrimpton [38]. Since cases S2 and S3 have higher electric Reynolds numbers, the flow mixing in the bulk area is better than in the other two cases. This is because cases S2 and S3 have lower dimensionless mobilities, and the electric field has less effect on charge transport, contributing less to the upward flow. Conversely, with larger mobilities, upward charge transfer is predominantly influenced by electric migration, and enhances the flow structures of higher charge transport efficiency. This is beneficial to form the charge void region as more charge plumes pass across the entire domain.

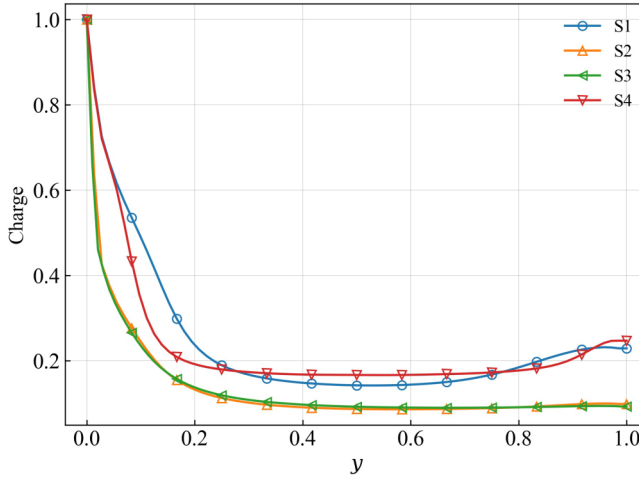


FIG. 11. The spatial and temporal averages of the horizontal direction of charge density.

Figure 11 illustrates the temporal average charge density across the entire horizontal direction. It is noticeable that the average charge density distributions in the S2 and S3 cases exhibit similarities, characterized by a sharply defined charge boundary layer and a flat bulk density profile. The charge boundary layer of case S1 is wider than the two mentioned cases, while the middle area charge density is nearly identical. In addition, case S1 has an additional increase in charge density close to the upper plate. Actually, the average feature of case S1 is more likely to appear in previous 2D results which have typical charge void cells. Because the injection strength of case S4 is smaller, the bulk charge density is higher and the charge density boundary layer is the widest among all cases. The average charge density computed in this work closely resembles that of Kourmatzis and Shrimpton [38], supporting the reliability of our LES model.

Figure 12 illustrates the kinetic energy spectrum in the middle-height plane. The turbulent kinetic energy is taken to be attributed to  $k$ . The spectrum is determined by taking the Fourier transform of velocity components  $u_x$  and  $u_z$  in the horizontal direction, multiplying by the complex conjugate,

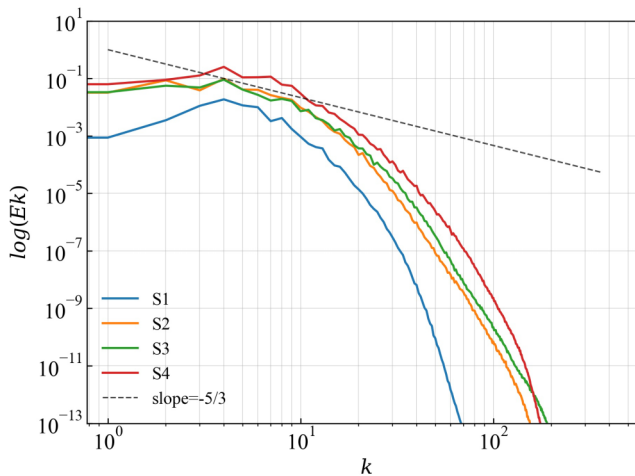


FIG. 12. Turbulent kinetic spectrum of horizontal velocity on the log-log scale at the mid-height slice. The  $k^{-5/3}$  spectrum is used to compare the inertial sub-range of the EC turbulence.

and taking the sum of energy contribution  $E(k)$  from each discrete node in the horizontal direction, where  $k$  is the wavenumber. The peak values of the energy spectrum of the cases are all in a similar scale, which indicates the general EC vortex scale distributions in the four cases are nearly identical. Furthermore, we observe a segment with a  $-\frac{5}{3}$  slope in all energy spectra, which is the character of 3D turbulence in the inertial subrange. It means that the electric force provides energy to the electrohydrodynamic flow and forms the large-scale EC vortices, which feed energy to the electrical turbulence, and the kinetic energy dissipates in the small scale eventually. Despite the relatively low Reynolds number in the S1 case, it exhibits a narrow  $-\frac{5}{3}$  slope spectrum, showing a feature of weak turbulence. The other three cases have a wider inertial subrange, suggesting the electric force generates stronger turbulence. The amplitude of the energy spectrum also reflects the horizontal fluctuation intensity. In the four sets of spectra, case S4 has a stronger horizontal mixing effect albeit the S2 and S3 cases have larger Re. Additionally, cases S3 and S2 display similar spectra although their Re difference is twice that of case S4. These indicate the Re may not be the only critical parameter in determining the EC turbulence.

At last, we discuss the influence of dimensionless parameters on the electrohydrodynamic turbulence. There is no doubt that Re, which is the combination of electric Rayleigh number  $T$  and dimensionless mobility  $M$ , is one of the decisive factors, the EC turbulence is more likely to happen at a high value of Re or  $T$ . The EC flow with a larger  $M$  number has a stronger electric migration ability. The electric force tends to form a charge void region in EC with a large  $M$  value. The parameter  $C$  determines the bulk charge density and the gradient of the charge boundary layer. Here we only give a primary discussion. To comprehensively compare the influence of dimensionless parameters, it needs a more systematic and in-depth study.

#### IV. CONCLUSION

Turbulent electric-driven flow is an important branch of EHD. This work attempts to adopt an LES turbulence model for numerical simulation of EC. In this paper, the LES eddy-viscosity method, including the Smagorinsky and WALE models, is incorporated into the LBM solver for simulating electrohydrodynamic flow. We simulate three cases of EC turbulence, including 2D turbulence in enclosed cells, and 3D large-scale EC between two parallel plates. For the 2D EC turbulence simulation, we compare the results obtained by various numerical methods. For the 2D EC turbulence simulation, we compare the results obtained by various numerical methods, including LBM-LES, LBM-DNS, SEM-DNS, and FVM-LES models. We find that the two LBM-LES models show reliable abilities to acquire the evolution of flow intensity and electric Nusselt number, and can capture the main flow patterns in 2D EC turbulence. The LES model can improve computing efficiency for electrohydrodynamic turbulence at least six- to eightfold compared to the LBM-DNS model. The LBM model can get at least sixfold speedup in computation compared to FVM using the same time step. Even using the adaptive time step in the FVM, the speedup of the LBM is still significant. And the computational efficiency of the LBM is higher in a larger scale of computation. Since the Smagorinsky model can be implemented in the LB collision step, the computational cost is a little lower than that of the WALE model. However, the WALE model has better accuracy because of the absence of wall eddy viscosity, simulating the transition stage from electric force dominant to inertial dominant regions better. Since the LBM method has a smaller numerical dissipation, it is possible to acquire more flow detail, which is slightly better than the performance of the FVM model with the same turbulence model. For 3D cases, the Smagorinsky model shows good reliability, including describing the flow states, probability density, average characteristics, and energy spectrum. Moreover, the 3D simulation also shows that EC turbulence not only has the general characteristics of hydrodynamic turbulence ( $-\frac{5}{3}$  slope kinetic energy spectrum) but also has similar flow scale distributions under different driven parameters.

This work may pave the way for electrohydrodynamic turbulence simulation with insufficient resolution. Developing reliable turbulence models for EHD and implementing them across multiple numerical methods are meaningful directions in the study of EC turbulence. Additionally,

some other advanced LES models and higher-order numerical methods, accumulating sufficient experimental results and implementing comparison, are also of great significance in the further investigation of EHD. Future work can focus on these aspects mentioned above.

#### ACKNOWLEDGMENTS

This work is supported by the National Natural Science Foundation of China (Grant No. 52076055), the Fundamental Research Funds for the Central Universities (Grants No. FRFCU5710051020 and No. HIT.DZJJ.2023104), and the CGN-HIT Advanced Nuclear and New Energy Research Institute (Grant No. MH20211181). The numerical computations were performed at Hefei Advanced Computing Center.

- 
- [1] S. B. Pope, *Turbulent Flows* (Cambridge University Press, Cambridge, UK, 2000).
  - [2] A. Belmonte, A. Tilgner, and A. Libchaber, Boundary layer length scales in thermal turbulence, *Phys. Rev. Lett.* **70**, 4067 (1993).
  - [3] B. Castaing, G. Gunaratne, F. Heslot, L. Kadanoff, A. Libchaber, S. Thomae, X.-Z. Wu, S. Zaleski, and G. Zanetti, Scaling of hard thermal turbulence in Rayleigh-Bénard convection, *J. Fluid Mech.* **204**, 1 (1989).
  - [4] H.-D. Xi and K.-Q. Xia, Flow mode transitions in turbulent thermal convection, *Phys. Fluids* **20**, 055104 (2008).
  - [5] D. Lohse and K.-Q. Xia, Small-scale properties of turbulent Rayleigh-Bénard convection, *Annu. Rev. Fluid Mech.* **42**, 335 (2010).
  - [6] K.-Q. Xia, Current trends and future directions in turbulent thermal convection, *Theor. Appl. Mech. Lett.* **3**, 052001 (2013).
  - [7] N. Foroozani, D. Krasnov, and J. Schumacher, Turbulent convection for different thermal boundary conditions at the plates, *J. Fluid Mech.* **907**, A27 (2021).
  - [8] D. Biskamp, *Magnetohydrodynamic Turbulence* (Cambridge University Press, Cambridge, UK, 2003).
  - [9] M. K. Verma, Statistical theory of magnetohydrodynamic turbulence: Recent results, *Phys. Rep.* **401**, 229 (2004).
  - [10] V. M. Uritsky, A. Pouquet, D. Rosenberg, P. D. Mininni, and E. Donovan, Structures in magnetohydrodynamic turbulence: Detection and scaling, *Phys. Rev. E* **82**, 056326 (2010).
  - [11] F. Plunian, R. Stepanov, and P. Frick, Shell models of magnetohydrodynamic turbulence, *Phys. Rep.* **523**, 1 (2013).
  - [12] J. Lacroix, P. Atten, and E. Hopfinger, Electro-convection in a dielectric liquid layer subjected to unipolar injection, *J. Fluid Mech.* **69**, 539 (1975).
  - [13] A. Castellanos, *Electrohydrodynamics*, Vol. 380 (Springer Science & Business Media, Vienna, Austria, 1998).
  - [14] P. Tsai, Z. A. Daya, and S. W. Morris, Aspect-ratio dependence of charge transport in turbulent electroconvection, *Phys. Rev. Lett.* **92**, 084503 (2004).
  - [15] P. Tsai, Z. A. Daya, and S. W. Morris, Charge transport scaling in turbulent electroconvection, *Phys. Rev. E* **72**, 046311 (2005).
  - [16] W. Zhao and G. Wang, Cascade of turbulent energy and scalar variance in DC electrokinetic turbulence, *Physica D* **399**, 42 (2019).
  - [17] A. Kourmatzis, E. L. Ergene, J. S. Shrimpton, D. C. Kyritsis, F. Mashayek, and M. Huo, Combined aerodynamic and electrostatic atomization of dielectric liquid jets, *Exp. Fluids* **53**, 221 (2012).
  - [18] A. Kourmatzis and J. Shrimpton, Electrohydrodynamic inter-electrode flow and liquid jet characteristics in charge injection atomizers, *Exp. Fluids* **55**, 1 (2014).
  - [19] C.-L. Lu, X.-L. Gao, J. Wu, K. Luo, and H.-L. Yi, Heat transfer enhancement analysis of electrohydrodynamic solid-liquid phase change via lattice Boltzmann method, *Appl. Therm. Eng.* **194**, 117112 (2021).

- [20] K. He, B. Ma, and L. Wang, Electrohydrodynamic enhancement of phase change material melting in cylindrical annuli under microgravity, *Appl. Therm. Eng.* **215**, 119005 (2022).
- [21] J.-D. Yao, K. Luo, J. Wu, and H.-L. Yi, Electrohydrodynamic effects on bubble dynamics during nucleate pool boiling under the leaky dielectric assumption, *Phys. Fluids* **34**, 013606 (2022).
- [22] K. McLean, Electrostatic precipitators, *IEE Proc. A Phys. Sci. Meas. Instrum. Manage. Educ. Rev. UK* **135**, 347 (1988).
- [23] K. Adamiak, Numerical models in simulating wire-plate electrostatic precipitators: A review, *J. Electrostat.* **71**, 673 (2013).
- [24] J. Tang, L. Gong, J. Jiang, Z. Li, and J. Han, Numerical simulation of electrokinetic desalination using microporous permselective membranes, *Desalination* **477**, 114262 (2020).
- [25] A. Mani and K. M. Wang, Electroconvection near electrochemical interfaces: Experiments, modeling, and computation, *Annu. Rev. Fluid Mech.* **52**, 509 (2020).
- [26] J. Seyed-Yagoobi, J. E. Bryan, and J. Castaneda, Theoretical analysis of ion-drag pumping, *IEEE Trans. Ind. Appl.* **31**, 469 (1995).
- [27] J. Seyed-Yagoobi, Electrohydrodynamic pumping of dielectric liquids, *J. Electrostat.* **63**, 861 (2005).
- [28] V. Cacciucolo, J. Shintake, Y. Kuwajima, S. Maeda, D. Floreano, and H. Shea, Stretchable pumps for soft machines, *Nature (London)* **572**, 516 (2019).
- [29] A. Castellanos, Coulomb-driven convection in electrohydrodynamics, *IEEE Trans. Electr. Insul.* **26**, 1201 (1991).
- [30] J. Wu, P. Traoré, P. A. Vázquez, and A. T. Pérez, Onset of convection in a finite two-dimensional container due to unipolar injection of ions, *Phys. Rev. E* **88**, 053018 (2013).
- [31] W. Zhao, General flux model in the turbulence driven by multiscale forces, *Phys. Rev. Fluids* **7**, 084607 (2022).
- [32] E. Hopfinger and J. Gosse, Charge transport by self-generated turbulence in insulating liquids submitted to unipolar injection, *Phys. Fluids* **14**, 1671 (1971).
- [33] X. Zhang, Electro-optic signatures of turbulent electroconvection in dielectric liquids, *Appl. Phys. Lett.* **104**, 202901 (2014).
- [34] S. Grossmann and D. Lohse, Scaling in thermal convection: A unifying theory, *J. Fluid Mech.* **407**, 27 (2000).
- [35] A. Varshney, S. Gohil, M. Sathe, S. R. RV, J. Joshi, S. Bhattacharya, A. Yethiraj, and S. Ghosh, Multiscale flow in an electro-hydrodynamically driven oil-in-oil emulsion, *Soft Matter* **12**, 1759 (2016).
- [36] G. Wang, F. Yang, and W. Zhao, Microelectrokinetic turbulence in microfluidics at low Reynolds number, *Phys. Rev. E* **93**, 013106 (2016).
- [37] W. Zhao and G. Wang, Scaling of velocity and scalar structure functions in AC electrokinetic turbulence, *Phys. Rev. E* **95**, 023111 (2017).
- [38] A. Kourmatzis and J. Shrimpton, Turbulent three-dimensional dielectric electrohydrodynamic convection between two plates, *J. Fluid Mech.* **696**, 228 (2012).
- [39] P. Traoré and A. Pérez, Two-dimensional numerical analysis of electroconvection in a dielectric liquid subjected to strong unipolar injection, *Phys. Fluids* **24**, 037102 (2012).
- [40] Q. Wang, Y. Guan, J. Huang, and J. Wu, Chaotic electro-convection flow states of a dielectric liquid between two parallel electrodes, *Eur. J. Mech. B Fluids* **89**, 332 (2021).
- [41] J. Huang, Q. Wang, Y. Guan, Z. Du, R. D. Selvakumar, and J. Wu, Numerical investigation of instability and transition to chaos in electro-convection of dielectric liquids between concentric cylinders, *Phys. Fluids* **33**, 044112 (2021).
- [42] Y. Zhang, D.-L. Chen, X.-P. Luo, K. Luo, J. Wu, and H.-L. Yi, Coulomb-driven electroconvection turbulence in two-dimensional cavity, *J. Fluid Mech.* **980**, A22 (2024).
- [43] A. Kourmatzis and J. Shrimpton, Turbulence closure models for free electroconvection, *Int. J. Heat Fluid Flow* **71**, 153 (2018).
- [44] J. Smagorinsky, General circulation experiments with the primitive equations: I. The basic experiment, *Mon. Weather Rev.* **91**, 99 (1963).
- [45] S. Hou, J. Sterling, S. Chen, and G. D. Doolen, A lattice Boltzmann subgrid model for high Reynolds number flows, [arXiv:comp-gas/9401004](https://arxiv.org/abs/comp-gas/9401004).

- [46] C. M. Teixeira, Incorporating turbulence models into the lattice-Boltzmann method, *Int. J. Mod. Phys. C* **09**, 1159 (1998).
- [47] M. Krafczyk, J. Tölke, and L.-S. Luo, Large-eddy simulations with a multiple-relaxation-time LBE model, *Int. J. Mod. Phys. B* **17**, 33 (2003).
- [48] F. Ducros, F. Nicoud, and T. Poinso, Wall-adapting local eddy-viscosity models for simulations in complex geometries, *Numerical Methods for Fluid Dynamics* (Springer, 1998), pp. 293–300.
- [49] P. Traoré, A. Pérez, D. Koulova, and H. Romat, Numerical modelling of finite-amplitude electro-thermo-convection in a dielectric liquid layer subjected to both unipolar injection and temperature gradient, *J. Fluid Mech.* **658**, 279 (2010).
- [50] J. Wu, P. Traoré, M. Zhang, A. T. Pérez, and P. A. Vázquez, Charge injection enhanced natural convection heat transfer in horizontal concentric annuli filled with a dielectric liquid, *Int. J. Heat Mass Transf.* **92**, 139 (2016).
- [51] K. Luo, J. Wu, H.-L. Yi, and H.-P. Tan, Lattice Boltzmann model for Coulomb-driven flows in dielectric liquids, *Phys. Rev. E* **93**, 023309 (2016).
- [52] Y. Guan and I. Novosselov, Two relaxation time lattice Boltzmann method coupled to fast Fourier transform Poisson solver: Application to electroconvective flow, *J. Comput. Phys.* **397**, 108830 (2019).
- [53] J. Huang, R. D. Selvakumar, Y. Guan, H. Li, P. Traoré, and J. Wu, Numerical investigation of injection-induced electro-convection in a dielectric liquid between two eccentric cylinders, *Int. J. Heat Fluid Flow* **83**, 108594 (2020).
- [54] K. He, L. Wang, and J. Huang, Electrohydrodynamic enhancement of phase change material melting in circular-elliptical annuli, *Energies* **14**, 8090 (2021).
- [55] S. Chen and G. D. Doolen, Lattice Boltzmann method for fluid flows, *Annu. Rev. Fluid Mech.* **30**, 329 (1998).
- [56] C. Obrecht, F. Kuznik, B. Tourancheau, and J.-J. Roux, Multi-GPU implementation of the lattice Boltzmann method, *Comput. Math. Appl.* **65**, 252 (2013).
- [57] A. Xu, L. Shi, and T. Zhao, Accelerated lattice Boltzmann simulation using GPU and OpenACC with data management, *Int. J. Heat Mass Transf.* **109**, 577 (2017).
- [58] A. Xu and B.-T. Li, Multi-GPU thermal lattice Boltzmann simulations using OpenACC and MPI, *Int. J. Heat Mass Transf.* **201**, 123649 (2023).
- [59] A. Xu and B.-T. Li, Particle-resolved thermal lattice Boltzmann simulation using OpenACC on multi-GPUs, *Int. J. Heat Mass Transf.* **218**, 124758 (2024).
- [60] C. K. Aidun and J. R. Clausen, Lattice-Boltzmann method for complex flows, *Annu. Rev. Fluid Mech.* **42**, 439 (2010).
- [61] T. Krüger, H. Kusumaatmaja, A. Kuzmin, O. Shardt, G. Silva, and E. M. Viggien, *The Lattice Boltzmann Method: Principles and Practice*, Graduate Texts in Physics (Springer International Publishing, Cham, Switzerland, 2017).
- [62] L. Jahanshaloo, E. Pouryazdanpanah, and N. A. Che Sidik, A review on the application of the lattice Boltzmann method for turbulent flow simulation, *Numer. Heat Transf. Part A: Appl.* **64**, 938 (2013).
- [63] K. J. Petersen and J. R. Brinkerhoff, On the lattice Boltzmann method and its application to turbulent, multiphase flows of various fluids including cryogenics: A review, *Phys. Fluids* **33**, 041302 (2021).
- [64] S. Chen, H. Liu, and C. Zheng, Numerical study of turbulent double-diffusive natural convection in a square cavity by LES-based lattice Boltzmann model, *Int. J. Heat Mass Transf.* **55**, 4862 (2012).
- [65] H. Liu, C. Zou, B. Shi, Z. Tian, L. Zhang, and C. Zheng, Thermal lattice-BGK model based on large-eddy simulation of turbulent natural convection due to internal heat generation, *Int. J. Heat Mass Transf.* **49**, 4672 (2006).
- [66] H. Wu, J. Wang, and Z. Tao, Passive heat transfer in a turbulent channel flow simulation using large eddy simulation based on the lattice Boltzmann method framework, *Int. J. Heat Fluid Flow* **32**, 1111 (2011).
- [67] S.-C. Chang, Y.-T. Yang, C.-K. Chen, and W.-L. Chen, Application of the lattice Boltzmann method combined with large-eddy simulations to turbulent convective heat transfer, *Int. J. Heat Mass Transf.* **66**, 338 (2013).
- [68] C. Zhuo and C. Zhong, LES-based filter-matrix lattice Boltzmann model for simulating turbulent natural convection in a square cavity, *Int. J. Heat Fluid Flow* **42**, 10 (2013).

- [69] Y. Wang, C. Shu, and C. Teo, Thermal lattice Boltzmann flux solver and its application for simulation of incompressible thermal flows, *Comput. Fluids* **94**, 98 (2014).
- [70] S. R. G. Polasanapalli and K. Anupindi, Large-eddy simulation of turbulent natural convection in a cylindrical cavity using an off-lattice Boltzmann method, *Phys. Fluids* **34**, 035125 (2022).
- [71] C. Flint and G. Vahala, A large eddy lattice Boltzmann simulation of magnetohydrodynamic turbulence, *Phys. Lett. A* **382**, 405 (2018).
- [72] M. Taha, S. Zhao, A. Lamorlette, J.-L. Consalvi, and P. Boivin, Lattice-Boltzmann modeling of buoyancy-driven turbulent flows, *Phys. Fluids* **34**, 055131 (2022).
- [73] Y. Zhang, D.-L. Chen, A.-J. Liu, K. Luo, J. Wu, and H.-L. Yi, Full bifurcation scenarios and pattern formation of laminar electroconvection in a cavity, *Phys. Fluids* **34**, 103612 (2022).
- [74] P. Traoré and J. Wu, On the limitation of imposed velocity field strategy for Coulomb-driven electroconvection flow simulations, *J. Fluid Mech.* **727**, R3 (2013).
- [75] J. Bardina, J. Ferziger, and W. Reynolds, Improved subgrid-scale models for large-eddy simulation, 13th Fluid, Plasmadynamics and Conference (unpublished), p. 1357.
- [76] Y. Tominaga and T. Stathopoulos, Turbulent Schmidt numbers for CFD analysis with various types of flowfield, *Atmos. Environ.* **41**, 8091 (2007).
- [77] Z. Guo, C. Zheng, and B. Shi, Discrete lattice effects on the forcing term in the lattice Boltzmann method, *Phys. Rev. E* **65**, 046308 (2002).
- [78] J. Latt, O. Malaspinas, D. Kontaxakis, A. Parmigiani, D. Lagrava, F. Brogi, M. B. Belgacem, Y. Thorimbert, S. Leclaire, and S. Li, Palabos: Parallel lattice Boltzmann solver, *Comput. Math. Appl.* **81**, 334 (2021).
- [79] H.-K. Jiang, Y. Zhang, Z.-Y. Zhang, K. Luo, and H.-L. Yi, Instability and bifurcations of electro-thermoconvection in a tilted square cavity filled with dielectric liquid, *Phys. Fluids* **34**, 064116 (2022).
- [80] Z. Chai and B. Shi, A novel lattice Boltzmann model for the Poisson equation, *Appl. Math. Model.* **32**, 2050 (2008).
- [81] M. Liu, X.-P. Chen, and K. N. Premnath, Comparative study of the large eddy simulations with the lattice Boltzmann method using the wall-adapting local eddy-viscosity and Vreman subgrid scale models, *Chin. Phys. Lett.* **29**, 104706 (2012).
- [82] C. Gkoudesnes and R. Deiterding, Verification of the WALE large eddy simulation model for adaptive lattice Boltzmann methods implemented in the AMROC framework, in *Cartesian CFD Methods for Complex Applications* (Springer, Berlin, 2021), pp. 123–144.
- [83] G. K. Batchelor, Small-scale variation of convected quantities like temperature in turbulent fluid Part 1. General discussion and the case of small conductivity, *J. Fluid Mech.* **5**, 113 (1959).
- [84] P. A. Davidson, *Turbulence: An Introduction for Scientists and Engineers* (Oxford University Press, Oxford, UK, 2015).
- [85] P. F. Fischer, An overlapping Schwarz method for spectral element solution of the incompressible Navier–Stokes equations, *J. Comput. Phys.* **133**, 84 (1997).
- [86] M. O. Deville, P. F. Fischer, and E. H. Mund, *High-Order Methods for Incompressible Fluid Flow*, Cambridge Monographs on Applied and Computational Mathematics (Cambridge University Press, Cambridge, UK, 2002).
- [87] S. Saha, P. Biswas, and S. Nath, A review on spectral element solver Nek5000, *AIP Conf. Proc.* **2336**, 030001 (2021).
- [88] Y. Zhang, H.-K. Jiang, K. Luo, T.-F. Li, J. Wu, and H.-L. Yi, Electro-thermo-convection in a high Prandtl number fluid: Flow transition and heat transfer, *Int. J. Heat Mass Transf.* **201**, 123630 (2023).
- [89] H. Jasak, OpenFOAM: Open source CFD in research and industry, *Int. J. Naval Architecture Ocean Eng.* **1**, 89 (2009).
- [90] P. Yang, Y. Peng, D. S. Ramachandran, A. K. Alkaabi, and J. Wu, Numerical analysis of electrothermoconvection of a dielectric nanofluid in a heated cavity, *Phys. Scr.* **99**, 065034 (2024).
- [91] K. Luo, J. Wu, H.-L. Yi, and H.-P. Tan, Three-dimensional finite amplitude electroconvection in dielectric liquids, *Phys. Fluids* **30**, 023602 (2018).
- [92] K. Luo, X.-L. Gao, X.-R. He, H.-L. Yi, and J. Wu, Formation of dissipative structures in a three-dimensional electro-thermo-convective flow, *Phys. Rev. Fluids* **7**, 043701 (2022).